Distribution of plasma in the Io plasma torus as seen by radio occultation during *Juno* Perijove 1

Phillip H. Phipps[1], Paul Withers[1,2], Dustin R. Buccino[3], Yu-Ming Yang[3]

[1]Department of Astronomy, Boston University, Boston, MA, USA.

[2]Center for Space Physics, Boston University, Boston, MA, USA.

[3]Jet Propulsion Laboratory, California Institute of Technology, Pasadena, CA, USA.

Abstract. The moon Io is the dominant plasma source for the Jupiter magnetosphere. The plasma is distributed into a torus of material around Jupiter, called the Io plasma torus. The *Juno* spacecraft performed its first perijove on 27 August 2016. During this time the spacecraft's X and Ka-band radio signals passed through the Io plasma torus. From the differential Doppler shift of the X and Ka-band frequencies we are able to determine the Io plasma torus total electron content. From the total electron content, we determine that the electron densities are larger than predicted from *Voyager*-based models by around 35±14 percent in the cold torus and 38±14 percent in the torus beyond 5.5 R_J. The ion temperatures were greater than predicted from the models by 44±15 percent in the cold torus, but consistent with models in the torus beyond 5.5 R_J. From the time of maximum total electron content, which is sensitive to the torus location, we also find the Io plasma torus equatorial plane appears to be tilted by about 1.5 degrees more than the nominal centrifugal equator tilt based on the tilt of a dipole magnetic field approximation. Different tilts were found for the cold torus and torus beyond 5.5 R_J.

1. Introduction

The bulk of the plasma in Jupiter's magnetosphere is contributed by volcanic activity on Io. This volcanic activity creates an atmosphere around Io that is then lost to Jupiter's magnetosphere [*Thomas et al.*, 2004; *Bagenal et al.*, 2017a]. The material then becomes ionized via electron collisions or charge exchange [*Smyth and Combi*, 1988; *Smyth*, 1992]. Once ionized this material becomes trapped on the magnetic field lines and swept into a torus around Jupiter [*Thomas et al.*, 2004]. This torus of material is called the Io plasma torus, henceforth called the IPT. The torus is centered on Io's orbit, which lies in the plane of Jupiter's rotational equator at around 5.89 Jupiter radii (R_J). The equator of the torus is tilted 2/3 of the way to the magnetic equator from the rotational equator [*Hill et al.*, 1974; *Dessler*, 2002; *Khurana et al.*, 2004]. The tilt of the magnetic equator with respect to the rotational equator is nominally 9.5 degrees [*Dessler*, 2002; *Bagenal et al.*, 2017a], thus making the tilt of the torus equator with respect to the rotational equator equal to 6.3 degrees. The torus equator is also called the centrifugal equator.

The material in the torus has been found to be distributed into three regions along the plane of the centrifugal equator. These regions are distinct in both temperature and density. From closest to furthest from Jupiter, these regions are called the cold torus, ribbon, and warm torus [*Bagenal and Sullivan*, 1981; *Thomas*, 1993; *Bagenal*, 1994]. The cold torus is centered around 5.23 R_J. The average densities are around 1000 cm^{-3} and ion temperatures are around 2–4 eV [*Thomas et al.*, 2004]. This region is believed to form from diffusion of ions towards Jupiter that rapidly cool radiatively [*Richardson et al.*, 1980]. Moving out radially we arrive at the ribbon centered at around 5.6 R_J. This region gets its name from the narrow region of bright [S II] emission found in ground-based observations [*Trauger*, 1984]. This region has a characteristic density of around 3000 cm^{-3}. The ion temperatures rapidly increase from 2–6 eV at around 5.0 R_J to around 70 eV at the orbit of Io (5.89 R_J) [*Thomas et al.*, 2004]. The outermost region extends from the orbit of Io (5.89 R_J) to around the orbit of Europa (9.38 R_J). This region is called the warm torus. The warm torus is characterized by a relatively stable ion temperature of around 70–100 eV and a decrease in electron density from around 2000 cm^{-3} at the orbit of Io to around 20 cm^{-3} at the orbit of Europa [*Bagenal and Sullivan*, 1981; *Bagenal*, 1994]. Material in the warm torus or ribbon not lost to charge exchange, the dominant loss mechanism, takes around 20–80 days to diffuse throughout the rest of the magnetosphere [*Bagenal and Delamere*, 2011; *Bolton et al.*, 2015].

During its encounter with Jupiter in 1979, *Voyager 1* demonstrated that propagation of radio signals through the Io plasma torus appreciably affects those radio signals [*Eshleman et al.*, 1979; *Levy et al.*, 1981; *Campbell and Synnott*, 1985] The *Ulysses* spacecraft, during its gravity assist of Jupiter in 1992, was the first spacecraft to perform a polar pass of Jupiter. *Ulysses* performed a radio occultation observation of the IPT during its flyby [*Bird et al.*, 1992, 1993]. A profile of the total electron content (TEC, often expressed in units of electrons/m^2 or el/m^2) of the IPT was derived from these observations. The TEC observations were broadly consistent with expectations based on *Voyager* in situ observations. *Bird et al.* [1993] inferred column densities and temperatures by comparison of TEC observations and models. The *Ulysses* results demonstrated that radio occultation observations by a Jupiter polar orbiter could provide useful information about the IPT.

The *Juno* spacecraft arrived in a polar orbit around Jupiter on 4 July 2016. During each perijove pass, radio signals between the spacecraft and Earth propagate through Jupiter's magnetosphere and the IPT.

Juno is the first spacecraft whose orbit permits it to conduct radio occultations of the Io plasma torus that sample only a single longitude sector. The *Voyager 1* radio occultation measurements were complicated by the spacecraft being within the torus during the occultation. The *Ulysses* radio occultation measurements were complicated by the spacecraft being beyond the far side of the torus during the occultation, so that its radio signals passed through the Io plasma torus at two distinct longitudes. By contrast, *Juno* radio signals during an occultation pass through one longitude sector only and the spacecraft never travels through the torus.

The theoretical study of *Phipps and Withers* [2017] showed that plasma in Jupiter's magnetosphere, predominantly the IPT, would affect received frequencies of *Juno*'s X and Ka-band radio signals [*Mukai et al.*, 2012; *Asmar et al.*, 2017; *Folkner et al.*, 2017]. *Phipps and Withers* [2017] predicted that a profile of the TEC of the IPT could be derived from *Juno* radio occultation observations. *Phipps and Withers* [2017] also showed that the cold torus could be identified in a *Juno* TEC profile, despite being a significantly smaller contributor than the warm torus, due to substantial differences between the scale heights of the regions. Detection of the cold torus in the TEC profile would determine the location of the cold torus, which *Bagenal* [1994] found to be dependent on the higher-order moments of the magnetic field.

The aim of this paper is to determine and interpret the IPT TEC profile from radio occultation observations during *Juno* Perijove 1 (PJ1). We discuss the *Juno* data in

Section 2, the TEC measured on PJ1 in Section 3, a comparison between model and data in Section 4, a fit to the data to extract parameters in Section 5, a discussion of comparison in Section 6, and a summary of results in Section 7.

2. *Juno* Perijove One Observations

Juno perijoves occur every ~53 days. The radio science data for this paper were acquired during *Juno* PJ1, which occurred on 27 August 2016 at 12:52 Barycentric Dynamical Time (13:44 UTC Earth Received Time). The spacecraft was occulted by the IPT for approximately two hours around perijove. During PJ1, the Jupiter-Sun angular separation was 22.6 degrees as seen from Earth. During PJ1, a NASA Deep Space Network (DSN) tracking station (DSS 55, a 34m antenna at the Madrid Deep Space Communications Complex) transmitted an X-band radio signal to the spacecraft. The local time at this antenna (Central European Summer Time) was 14:44 at the time of PJ1. This radio signal was received and coherently re-transmitted by the spacecraft at X and Ka-band (the radio science system is discussed in *Asmar et al.* [2017]). Upon receipt at Earth, these radio signals were analyzed in support of *Juno* gravity science objectives [*Folkner et al.*, 2017]. The differential Doppler shift of the received radio signals (defined in Equation 1) was used by *Folkner et al.* [2017] to characterize the contribution of plasma to noise in the gravity science results. *Phipps and Withers* [2017] showed that this differential Doppler shift could also be used as a diagnostic of plasma densities in the IPT. Here we analyze the time series of received X and Ka-band frequencies, which are archived on the NASA Planetary Data System [*Buccino*, 2016].

The reconstructed orbit of the spacecraft around perijove is shown in Figure 1. A centrifugal cylindrical polar coordinate system is used with origin at the center of mass of

Jupiter. It is constructed so that a two-dimensional view in this coordinate system provides a useful representation of the positions of Io, the IPT, Jupiter, *Juno*, and Earth. The centrifugal reference frame's z-axis is aligned perpendicular to the nominal equatorial plane of the IPT. As discussed in Section 1, this axis is two-thirds of the way from the rotational pole to the magnetic pole, giving a tilt of approximately 6.3 degrees relative to the rotational pole. In the standard "System III" representation of Jupiter's rotational reference frame, which is a left handed reference frame, this axis has a longitude of 200.8 degrees [*Connerney et al.*, 1998; *Bagenal et al.*, 2017a].The x-axis is fixed to the intersection of the geographic and magnetic equators, and is situated at a System III longitude of 290.8 degrees.The y-axis completes the basis of the right-handed system. Note that, due to the usage of a cylindrical polar coordinate system for interpretation of observations, subsequent uses of "radial distance" should be interpreted as the length of the cylindrical radial coordinate. That is, distance from the z-axis of the frame, rather than distance from the origin. This frame is based on the VIP4 frame [*Connerney et al.*, 1998; *Bagenal et al.*, 2017a] with the torus tilt of 6.3 degrees substituted for the magnetic dipole tilt of 9.5 degrees.

Note that the tilt of centrifugal equator is based upon a dipole approximation of the magnetic field, specifically the dipole longitude and tilt from VIP4 [*Connerney et al.*, 1998; *Bagenal et al.*, 2017a]. Therefore this frame ignores possible effects of the higher moments of the magnetic field and any other magnetospheric processes on the centrifugal equator.

3. Perijove one total electron content

3.1. Total electron content from frequency observables

Conversion from the received frequency data to TEC values uses the following equation from *Phipps and Withers* [2017]:

$$\Delta f = f_{R,X} - f_{R,Ka}\left(\frac{f_{D,X}}{f_{D,Ka}}\right) = \frac{e^2}{8\pi^2 m_e \epsilon_0 c f_{T,X}}\left(1 - \left(\frac{f_{D,X}}{f_{D,Ka}}\right)^2\right)\frac{d}{dt}\int N dl. \quad (1)$$

The first equality defines Δf, the "differential Doppler shift". Here f is frequency, subscripts R and T refer to received and transmitted, respectively, subscript X refers to X-band, subscript Ka refers to Ka-band, c is the speed of light, t is time, l is distance along the ray path, $-e$ is the electron charge, m_e is the electron mass, ϵ_0 is the permittivity of free space, N is the electron density, and $\frac{f_{D,X}}{f_{D,Ka}}$ is the ratio of downlinked X-band frequency to the downlinked Ka-band frequency. In the coherent dual-frequency mode used in PJ1, this ratio is a fixed value of $\frac{880}{3360}$, or 11/42 [*Mukai et al.*, 2012; *Asmar et al.*, 2017]. However, this expression neglects the spin of the spacecraft (∼2 revolutions per minute [*Bolton et al.*, 2017]). As described for *Ulysses* by *Bird et al.* [1993], to include the effects of spacecraft spin, the quantity $\left(1 - \left(\frac{f_{D,X}}{f_{D,Ka}}\right)\right) f_{spin}$, which equals 0.0246 HZ, must be subtracted from Δf in Equation 1. The corrected time series of differential Doppler shift is shown in Figure 2 at 10 second resolution. Note that the time resolution of 10 seconds is similar to the 36 seconds assumed by *Phipps and Withers* [2017]. The noise in the observations at 10 seconds time resolution (1.1×10^{-3} Hz) is ∼ 3 times larger than predicted in *Phipps and Withers* [2017] (3.8×10^{-4} Hz). This difference is due to the solar wind and other noise sources neglected by *Phipps and Withers* [2017], who considered only the frequency stability of the DSN. The troposphere was determined to be the dominant noise source during PJ1 [*Folkner et al.*, 2017].

We integrate Equation 1 with respect to time to find $\int N dl$, which is the total electron content (TEC) along the Juno-Earth line of sight, as a function of time. The initial condition for TEC was chosen for consistency with the TEC contributed by Earth's ionosphere at this time (Section 3.2). Results are shown in Figure 3 (left panel). The IPT is clearly visible as an increase in TEC of about 35×10^{16} m^{-2} above background between 13 and 15 hours Earth Received Time. However, significant contributions from various background sources of plasma are also visible. These non-IPT contributions must be characterized and removed.

The error on the data, σ_{TEC}, is given by (from *Phipps and Withers* [2017])

$$\left(\frac{\sigma_{TEC}}{1\ \mathrm{TECU}}\right) = 1275 \frac{\sigma_{\Delta f}}{1\ \mathrm{Hz}} \sqrt{\left(\frac{t}{1\ \mathrm{hr}}\right)\left(\frac{\Delta t}{10\ \mathrm{s}}\right)}. \quad (2)$$

Where one total electron content unit (TECU) equals 10^{16} el/m^2 [*Mendillo et al.*, 2004], t is time since the start of the integration, and Δt is the time resolution (10 seconds). This equation defines the error on the uncalibrated data (gray region in left panel of Figure 3). The standard deviation of Δf at 10 second integration time at periods outside the window affected by the IPT (before 13 hours and after 15 hours Earth Received Time) is 1.1×10^{-3} Hz. We adopt this value as $\sigma_{\Delta f}$, the uncertainty in Δf.

3.2. Background calibration

The background TEC apparent in Figure 3 comes from different areas of the space environment. Two main contributions are Earth's ionosphere and the solar wind plasma in interplanetary space.

The TEC contribution from Earth's ionosphere along the line-of-sight between the ground station and the spacecraft is determined using GPS sensors at the ground station. These continuously measure the TEC between the ground station and GPS satellites in Earth orbit. A time series model of the line-of-sight TEC of Earth's ionosphere has been developed from these observations. This is provided in .ION ancillary files that accompany the archived frequency measurements in the Planetary Data System. These files provide line-of-sight range delay, RD, in units of meters at a reference S-band frequency of 2.295 GHz, from which TEC can be calculated [*Machuzak*, 2008]. For the duration of PJ1, the range delay RD in units of meters can be approximated by the following polynomial:

$$RD = 1.5829 + 0.7842X + 0.1171X^2 - 2.066X^3 + 1.5420X^4 \tag{3}$$
$$+6.9640X^5 + 1.7496X^6 - 8.9347X^7 - 2.1216X^8 + 3.8673X^9.$$

Here X at $time$ is defined by $2\frac{time-start}{end-start} - 1$ where $start$ and end are the start and end times of the range of times where this function is applicable for ionospheric calibration [*Machuzak*, 2008]. For the time span of PJ1, $start$ equals 29040 seconds past midnight (8:04:00 UTC) and end equals 69780 seconds past midnight (19:23:00 UTC). The ionospheric line-of-sight TEC in units of TECU equals $\frac{RDf_{ref}^2}{0.403}$, where f_{ref} is the reference S-band frequency of 2.295 GHz, RD is expressed in units of meters and f_{ref} is expressed in units of GHz [*Mendillo et al.*, 2004]. The ionospheric TEC found from Equation 3 is the cyan dashed curve shown in the left panel of Figure 3. This provided the initial condition used for the initial TEC integration (Section 3.1). The significant increase in ionospheric TEC at the end of the observing period is caused by the spacecraft elevation approaching the horizon, which increases the path length through Earth's ionosphere. The observed TEC corrected for Earth's ionosphere is shown in the middle panel of Figure 3. To account for error in the calibration we adopt an error of around 2 TECU on the ionosphere [*Thornton and Border*, 2000]. Using general error propagation methods gives an error on the data shown as the gray shaded region on the data in the middle panel of Figure 3. Note that negative values of TEC seen in the middle panel of Figure 3 indicate that some additional background contribution to the observed TEC decreases with time, they should not be interpreted as true negative total electron content.

A background contribution to TEC that decreases with increasing time remains after the ionospheric correction. We interpret this as variations in solar wind conditions between Earth and Jupiter. During the occultation the Jupiter-Earth-Sun angle was 22.6 degrees. The distance from Earth to Jupiter was 6.37 AU. This background contribution must be removed in order to isolate the IPT TEC. Following the method used for the ionospheric correction, we fit a ninth order polynomial function of time to the corrected TEC outside the fiducial range of 13.16 to 15.06 hrs. This excludes the contributions of the IPT. The resultant fit to the background TEC in TECU is:

$$Background\ TEC = -7.171 - 7.446\ T - 4.754\ T^2 + 17.34\ T^3 + 12.01\ T^4 \\ -17.71\ T^5 - 4.957\ T^6 + 9.278\ T^7 + 0.5715\ T^8 - 1.751\ T^9. \quad (4)$$

Here T is $\frac{time-5.446\times10^4}{9284}$ where *time* is in seconds past midnight, 5.446×10^4 seconds is the mean of the times of the fitted data, and 9284 seconds is the standard deviation of the times of the fitted data. This background calibration is shown by the red dotted line in the middle panel of Figure 3. The complete calibrated TEC after subtraction of this background is shown in the right panel of Figure 3. We assume that the IPT is the sole contributor to this calibrated TEC profile. The uncertainty is assumed to be unchanged after the correction for non-ionosphere background plasma (gray shaded region on right panel of Figure 3). The average error over the observing period is 3.38 TECU with standard deviation of 0.69 TECU.

In the right panel of Figure 3, note that the scatter of the TEC values is appreciably smaller than the reported TEC uncertainties. Clearly the scatter in the TEC values does not arise from uncorrelated measurements sampled from a normal distribution with standard deviation equal to the reported uncertainty. Since TEC is an integrated quantity, the background TEC measurements are not uncorrelated. The peak TEC of the IPT (shown in the right panel of Figure 3) is 36.8 ± 2.1 TECU located at 13.93 ± 0.02 hours. These peak properties and their uncertainties were found by a Monte Carlo approach with an ensemble size of 10,000. Each Δf data point was modified by the addition of a value drawn from a normal distribution with mean zero and standard deviation equal to $\sigma_{\Delta f}$. The reported peak TEC and its uncertainty are the mean and standard deviation of the ensemble of peak TEC values. The reported peak time and its uncertainty are the mean and standard deviation of the ensemble of times of peak TEC value. The peak TEC value of 36.8 ± 2.1 TECU found for Perijove 1 is consistent with the *Ulysses* peak TEC value of approximately 60 TECU along a line of sight that passed through the torus twice [*Bird et al.*, 1993].

4. Perijove 1 comparison to *Voyager* models

Here we compare the TEC results to models based on *Voyager* in situ data.

4.1. Update to *Phipps and Withers* [2017] model parameters

We begin with the empirical model of *Phipps and Withers* [2017] (their Equations 15–16 and their Table 2), which provides electron density as a function of position. We label this Model A. The functional form of this model is a piece-wise function in the torus equatorial plane . For radial distances less than 6.10 R_J, electron density is given by a sum of three Gaussians, one each for the cold torus, ribbon, and warm torus. For radial distances greater than 6.10 R_J, electron density is given by the tail of a single Gaussian representing the extended torus. The central densities, peak locations, and peak widths each of the Gaussian functions were found from a fit to *Voyager* in situ data. Outside the torus equatorial plane, densities are found using the scale height approximation to the diffusive equilibrium equation for a multi-species plasma. The scale heights for the cold torus, ribbon, warm torus, and extended torus are independent. [*Phipps and Withers*, 2017].

We modify Model A to account for a recent reanalysis of the *Voyager* data by *Bagenal et al.* [2017b]. Model scale heights are updated due to composition and temperature changes found by *Bagenal et al.* [2017b] and *Nerney et al.* [2017]. Model densities are updated due to reanalysis of *Voyager* data by *Bagenal et al.* [2017b]. Modified model parameters are shown in Table 1. We label this Model B.

4.2. Model Comparison to data

Models predict density as a function of position, whereas the data measure TEC as a function of Earth Received Time. To compare models to data, we find the line-of-sight between Earth at the Earth Received Time and the spacecraft at the earlier transmission time, then integrate the model electron density along this line-of-sight. This provides a model value of TEC at this Earth Received Time. Repetition for all Earth Received Times provides a model time series of IPT TEC as a function of Earth Received Time. We use the NAIF SPICE tools to do this, accounting for the light travel time between

Juno and Earth. TEC predictions from Model B are shown in Figure 4 alongside the observed TEC. The major impression from this comparison is that the predicted peak TEC of Model B is significantly less than the observed peak TEC.

Predicted and observed peak TEC agree well if all densities in Model B are increased by a factor of 1.37, as shown in Figure 5. We label this rescaling of Model B as Model C. It should be noted here that the observed time series of TEC is quite insensitive to the radial distribution of plasma. Consequently, interpretation of the observed TEC in terms of local plasma density in the IPT requires assumptions about the radial structure of the IPT. Models A—C adopt the radial distribution of plasma found during the *Voyager* epoch. With that caveat, this scaling factor suggests that IPT densities were around 37 percent larger during PJ1 than during the *Voyager* epoch.

The Model C-data residuals shown in Figure 5 show systematic behavior. TEC values predicted by Model C are systematically larger than observed TEC values at early times, then systematically smaller at later times. Equivalently, the peak TEC predicted by Model C occurs 2.4 minutes before the peak observed TEC. One possible explanation for this feature is that the plane of the IPT is tilted with respect to the rotational equator by an angle that differs from the nominal 6.3 degrees. Here we consider how changes in the tilt of the plane of the IPT would affect observed TEC values.

For the PJ1 geometry, if the tilt of the plane of the IPT with respect to the rotational equator is decreased from the nominal 6.3 degrees, then the peak TEC would occur earlier in the observations. Similarly, if the tilt of the plane of the IPT with respect to the rotational equator is increased from the nominal 6.3 degrees, then the peak TEC would occur later in the observations. Therefore we adjusted the IPT tilt in Model C and monitored how this affected the model-data residuals. As the IPT tilt in Model C was increased from the nominal value of 6.3 degrees from the rotational equator, the model-data residuals diminished to a minimum, then increased. The residuals appeared to be minimized at a tilt of 7.8 degrees from the rotational equator. This is illustrated in Figure 6, which shows Model C (tilt of 6.3 degrees, nominal value), Model D (tilt of 7.8 degrees, aligns model and observed times of peak TEC), and Model E (9.5 degrees, plane of magnetic equator). Model-data residuals show systematic behavior for Models C (6.3 degrees) and E (9.5 degrees), but are smaller and scattered around zero for Model D (7.8 degrees). This illustrates that an adjusted tilt of the plane of the IPT provides significantly better agreement between model and observations. With that principle established, we now refine the value of the tilt implied by the time of peak TEC.

The observed time of the peak TEC is 13.93 ± 0.02 hours. The corresponding model tilt that matches the time of peak TEC is 7.5 ± 0.4 degrees, which is 1.2 ± 0.4 degrees greater than the nominal tilt of 6.3 degrees. This is consistent with the 7.8 degrees suggested by the preceding visual inspection of the residuals. We hypothesize that the slight difference between the results of 7.8 degrees and 7.5 degrees arises because the inspection of residuals was most sensitive to the properties of the warm torus, whereas matching the precise time of peak TEC was most sensitive to the location of the cold torus.

Another possible explanation for the discrepancy in the time of peak TEC is that the longitude of the pole of the IPT is different from its nominal value. The nominal value is the same as the System III longitude of the magnetic pole, 200.8 degrees, where the relevant coordinate systems are discussed further in *Bagenal et al.* [2017a]. To explore this possibility, we allowed the pole longitude in Model C, which has the nominal tilt of

6.3 degrees, to rotate around Jupiter. After a complete revolution around Jupiter, the resultant Earth Received Time of peak TEC in the model varied between a minimum of 13.49 hours at 20.8 degrees and a maximum of 13.90 hours at 210.8 degrees. For the nominal pole longitude of 200.8 degrees, the Earth Received Time of peak TEC in the model was 13.89 hours. Recall that the observed time of peak TEC is 13.93 ± 0.02 hours. Although changes in pole longitude can affect the Earth Received Time of peak TEC considerably, such changes cannot significantly improve the agreement between model and data for the PJ1 observations. Given this result, we do not explore sensitivity to changes in both tilt and pole longitude.

The Io plasma torus is believed to lie in the centrifugal equator, meaning the locus of points that are the farthest away from Jupiter on a given field line. If the magnetic field is purely dipolar, then the centrifugal equator is a plane. Futhermore, this plane is tilted with respect to the plane of the rotational equator by two-thirds of the tilt between the rotational and magnetic equators, as discussed previously. However, if the magnetic field possesses higher-order terms and is not purely dipolar, then the centrifugal equator may not be a plane and the tilt of a plane fitted to the centrifugal equator may not be the same as for the dipole-only case. In the above analysis, we have used pole longitude and dipole tilt for the magnetic dipole approximation of the VIP4 model (see Section 2). More realistic descriptions of the centrifugal equator based upon more realistic magnetic field models may be valuable for interpreting the implications of the time of peak TEC of the IPT that was observed on PJ1. For example, the VIP4 model [*Connerney et al.*, 1998] contains higher-order components of the magnetic field that are not included in the simple dipole approximation used here. Other field models, such as VIPAL [*Hess et al.*, 2011] and the empirical model of *Grodent et al.* [2008], use modifications to the VIP4 model to match auroral observations [*Bagenal et al.*, 2017a]. Furthermore, the unprecedented magnetic measurements of *Juno* will lead to the development of a new magnetic field model that is likely to replace pre-*Juno* models in most applications.

Along with dipole tilt and pole longitude, it is also possible to change the time of peak TEC with a longitudinal variation in density. We used a sinusoidal variation in density of $ne\left(r, \lambda_{III}\right) = ne\left(1 + Asin\left(\left(\lambda_{III} - \lambda_0\right)\frac{\pi}{2}\right)\right)$ with A equal to 0.5. This sinusoidal variation reproduces the variation found by *Steffl et al.* [2008] with a larger amplitude of variation. With the fifty percent variation in density the time of peak TEC is shifted from 13.89 hours to around 13.90 hours but during this time the peak TEC was increased by 50 percent. To account for the 37 percent increase in density we use $A = 0.37$. With the 37 percent increase in density the peak TEC is the same as that of the data but the time of peak TEC is only moved to 13.897 hours. Thus, this can account for the density increase but is not a reasonable explanation for the difference in time of peak TEC.

5. Determining parameters from the data

We now fit the observed TEC directly. In order to place our observations in a general context, we fit the TEC as a function of position, not of Earth Received Time.

5.1. Fit to the data

For a given Earth Received Time, the position coordinate used is the z-coordinate of the point along the *Juno*-Earth line-of-sight whose value of $\sqrt{x^2 + y^2}$ equals 5.89 R_J, the orbital distance of Io. Here x, y, and z are expressed in the centrifugal coordinate system introduced in Section 2. In this system, the nominal plane of the IPT is the $z = 0$

plane. We fit the observed TEC using the sum of multiple Gaussian functions. *Phipps and Withers* [2017] discussed the suitability of this functional form for IPT observations. Using simulated data, they showed that the peak TEC and scale height can be determined from TEC profiles of the torus using a sum of Gaussians, one for each of the three distinct torus regions. The final fit to the simulated data had a reduced χ^2 of 1.004. It was also shown that, since the three regions are distinct in both temperature and density, each parameter of the Gaussian function has an independent effect on the profile.

In contrast to the three Gaussians of *Phipps and Withers* [2017], here we use only two Gaussians. There is no clear signature of the narrow ribbon in the TEC observations from PJ1. This is a consequence of the observational geometry. The ribbon and the warm torus have similar scale heights. The primary difference in their electron density distributions is that the ribbon is confined to a narrow range of radial distances (e.g., width of 0.08 R_J in Model A). These occultation observations integrate density along a line of sight. Therefore, they are relatively insensitive to the distinction between the ribbon and the warm torus. Thus the fit function is

$$TEC(z) = a_1 e^{-(z-b_1)^2/c_1^2} + a_2 e^{-(z-b_2)^2/c_2^2}, \tag{5}$$

where a_n is the peak TEC, b_n is the peak location offset, and c_n is the scale height. With the convention that the Gaussian with the smaller fitted scale height represents the cold torus, here the subscript 1 refers to the cold torus and 2 to the combination of the ribbon, warm torus, and extended torus. Based on the locations of these regions in the Voyager-era observations, for convenience we refer to the contribution marked with subscript 2 as "the torus beyond 5.5 R_J". The physical significance of fit parameters a_n (peak TEC) and c_n (scale height) are self-explanatory. The physical significance of fit parameters b_n, called the peak location offset, is that b_n represents the offset of peak TEC above or below the nominal plane of the centrifugal equator. In the limit of lines of sight parallel to the centrifugal equator, non-zero values of b_n can be interpreted as the torus being displaced from its predicted location in the nominal centrifugal equator.

We find the set of parameters that minimizes the χ^2 between the time series of observed and modeled TEC. We perform the fit using a Markov Chain Monte Carlo (MCMC) python routine assuming a normal distribution for the parameters [*Foreman-Mackey et al.*, 2013]. 7×10^4 runs were performed, and the resultant best fit values and their uncertainties are reported in Table 2. We label this as Model F. The reduced χ^2 for the MCMC fit was 1.04. Note that Models A—E are based on Voyager in situ data, whereas Model F is based on *Juno* radio occultation data.

The MCMC fit routine requires initial values for all fit parameters. These were obtained by fitting the same functional form to the observed TEC values as a function of the z position of the *Juno*-Earth line-of-sight, at a radial distance of 5.89 R_J in centrifugal coordinates, using the MatLab curve fitting tool (the root-mean-square error of the fit was 0.378 TECU) . These initial parameter values are also reported in Table 2. Figure 7 shows observed and Model F TEC(z).

We can compare these fit parameters to those predicted based on existing models. We use Model B (Table 1), which has the nominal torus tilt of 6.3 degrees, to predict TEC(z), then fit the predicted TEC(z) using Equation 5. The parameters a_n, b_n, and c_n found from this fit to Model B are those that would be predicted if the torus was located on the nominal centrifugal equator with the density distribution from the *Voyager* epoch. Results from this fit to Model B are listed in the first row of Table 2.

5.2. Interpretation of fitted total electron content

The TEC from Model B and Model F (fit to *Juno* data from PJ1) can be directly compared. The best fit TEC values a_1 and a_2 are shown in Table 2. The predicted value for a_1 from Model B is 5.23 TECU. The value found for Perijove 1 is 35±14 percent larger. The predicted value for a_2 from Model B is 21.7 TECU. The value found for Perijove 1 is 38±14 percent larger. Thus, the TEC of the IPT is increased by an average of 37 ± 14 percent. This is consistent with the result found in Section 4.2 by scaling the TEC profile from Model B to match the peak observed TEC.

5.3. Interpretation of fitted peak offset values

The peak offset values b_1 and b_2 are shown in Table 2. Even though Model B was defined to be symmetric about the centrifugal equator, the associated peak offset values are non-zero. Specifically, the peak offset values for Model B are 0.050 R_J for b_1 and -0.042 R_J for b_2. These non-zero values are artifacts of the geometry between the *Juno*-Earth lines-of-sight and the Io plasma torus (shown in Figure 1). The lines-of-sight are not parallel to the nominal centrifugal equator. When the line of sight passes through the nominal centrifugal equator at $\sqrt{x^2+y^2} = 5.89 R_J$, the radial distance of the peak of the warm torus, *Juno* is at $\sqrt{x^2+y^2}$ = 1.01 R_J and z = -0.457 R_J. Therefore this line of sight is at an angle of -5.4 degrees to the nominal centrifugal equator. Consequently, the line of sight through Model B that has the greatest cold torus TEC passes through the nominal centrifugal equator at a radial distance of 5.36 R_J. The line of sight through

Model B that has the greatest contribution from the torus beyond 5.5 R_J passes through the nominal centrifugal equator at 6.33 R_J. These values were used when calculating the tilts below.

The torus being distributed along the torus equator means the lines-of-sight will pass through the torus equator for a region closer to Jupiter at a different time than the regions further from Jupiter (for reference see Figure 1). During PJ1, the torus was near maximum tilt below the rotational equator. This leads to the lines-of-sight passing through the cold torus first and then the regions beyond. In the frame used for the Gaussian fit this results in the cold torus having a positive offset since it passes through the torus equator at an earlier time and occurs on an earlier line-of-sight. The peak TEC line-of-sight has a negative offset because it passes through the torus equator at a later time and thus occurs on a later line-of-sight.

The peak offset values found for Perijove 1 (Model F) are different from those for Model B. These differences illustrate that the regions of the Io plasma torus were not located in the nominal plane of the centrifugal equator at the time and place of these observations. This can be interpreted as differences from the nominal tilt of 6.3 degrees.

The difference between predicted positions and fitted positions (Table 2) gives the shift in the torus regions. Δb_1 is -0.088 ± 0.004 R_J while Δb_2 is -0.185 ± 0.024 R_J. These values give the offset from nominal torus location. For each region the corresponding offset from nominal torus tilt can be calculated using $\alpha_n = arcsin\left(\frac{\Delta b_n^2}{\mathrm{R_n}}\right)$ (see Figure 8). Here α_n is the angle from nominal torus tilt angle in degrees for the corresponding region (1 for cold torus and 2 for warm torus). R_n is the radial peak location of the cold torus and the torus beyond 5.5 R_J (5.36 and 6.33 R_J discussed above). With R_n and the Δb_n's above we can derive the offset tilt angle for each of the torus regions. The angles are 0.9±0.1 degrees for the cold torus and 1.7±0.2 degrees for the torus beyond 5.5 R_J. This can be interpreted as a tilt of the equatorial plane from the rotational equator of 7.2±0.1 degrees for the cold torus and 8.0±0.2 degrees for the warm torus. The average weighted by the peak TEC values gives an angle of 1.6 degrees. This is similar to the angle of 1.5 degrees found above by testing the tilt in the SPICE toolkit.

5.4. Interpretation of fitted scale heights

The scale heights c_1 and c_2 are shown in Table 2. The cold torus scale height found for Perijove 1 is 44±15 percent larger than predicted from Model B, but is similar to those found by Earth-based observations made after *Voyager* [*Thomas et al.*, 2001, 2004; *Nozawa et al.*, 2004]. The scale height found for the torus beyond 5.5 R_J in Perijove 1 is 2± 9 percent larger than predicted from Model B, which is not statistically different. It is also similar to results from Earth-based observations [*Thomas et al.*, 2001, 2004; *Nozawa et al.*, 2004]. It should be noted that the Model B scale heights reported in Tables 1 and 2 differ. This is because the values reported in Table 1 are the true scale heights, whereas those reported in Table 2 are those obtained by a fit to the TEC(z) appropriate for the occultation geometry of PJ1 in which the lines-of-sight are not parallel to the nominal centrifugal equator.

6. Discussion

Radio occultation observations during PJ1 have provided a profile of the TEC of the IPT at a longitude of 184 degrees (System III) and Earth Received Time of 13:54 UTC on 27 August 2016. The above longitude is for the time of peak TEC with range from 157 degrees at 12:54 UTC to 232 degrees at 14:54 UTC. The observed time of peak TEC was 0.04 hours, or 144 seconds, later than would have been seen if the IPT had been symmetric about the nominal plane of the centrifugal equator, which is tilted by 6.3 degrees relative to the rotational equator. This could be explained by the plane of the IPT having a different tilt of 7.8 degrees. Changes in the longitude of the pole of the plane of the IPT cannot resolve this discrepancy. The nominal tilt of 6.3 degrees is predicted for a dipole-only magnetic field. *Bagenal* [1994] found that inclusion of higher-order moments, and the magnetic field model used to provide those higher-order moments, affected the torus geometry. In the future, interpretation of the TEC observed on PJ1 in the context of more sophisticated descriptions of the predicted torus location will better constrain the structure and location of the Io plasma torus. We eagerly anticipate the development of a magnetic field model from the *Juno* spacecraft's magnetic field measurements.

Prior observations have discussed a difference in tilt of the ribbon and the cold torus [*Herbert et al.*, 2008]. *Herbert et al.* [2008] interpreted these observations as the cold torus being in the centrifugal equator and the ribbon being displaced from the centrifugal equator. However, the observations of *Juno* appear to show that all regions of the torus are displaced from the nominal plane of the centrifugal equator when using the dipole magnetic field approximation. Furthermore, *Juno* PJ1 radio occultations suggest that there is a difference in the tilts of the cold torus and the torus beyond 5.5 R_J. Earlier work has considered the possibility of torus tilts that differ from the nominal 6.3 degrees. *Bird et al.* [1993] found that a centrifugal equatorial tilt of 7.7 degrees created better agreement between the *Ulysses* TEC data and *Voyager* era models.

Model F has been derived from the PJ1 observations. However, Model F provides TEC, not local density as a function of position. In order to present a model of plasma density in the IPT as a function of position that is constrained by the PJ1 observations, we rescale the density and scale height parameters defined for Model B in Table 1 based on the density and scale height parameters found for the fit to PJ1 observations (Model F, Table 2). We label this final model as Model G, whose parameters are reported in Table 3. For Model G we use the different tilts found in each region to determine the $z = 0$ plane for the density distribution. Thus, the scale height distribution in the model is offset by a value equivalent to the predicted-fitted value for each the cold torus and torus beyond 5.5 R_J (Ribbon, Warm torus, and Extended torus).

The fitted peak TECs for the cold torus and the torus beyond 5.5 R_J were 35±14 percent and 38±14 percent, respectively, greater for Model F than Model B. This can be interpreted as the densities in the IPT at the time and place of the PJ1 occultation observations being greater than predicted in Model B. Consequently, the reference density for the cold torus is 35±14 percent greater for Model G than Model B and the reference densities for the ribbon, warm torus, and extended torus are 38±14 percent greater for Model G than Model B. *Bird et al.* [1993] interpreted the *Ulysses* measurements, which sampled two different longitude sectors of the torus, one sector had 50 percent larger densities and the other sector had around 30 percent smaller densities than *Voyager* based models. During the *Cassini* pass of Jupiter the torus was measured longitudinal and temporal variations in density of 10–40 percent [*Steffl et al.*, 2008]. *Thomas et al.* [2001] showed, using ground based data, that during a *Galileo* pass near Io the torus densities in the ribbon region were almost 50 percent higher than during the *Voyager* pass through the torus. A study using ground based observations from 1997 through 2000 show that the torus emissions, which can be related to the torus densities, varied by up to 50 percent over the three year period [*Nozawa et al.*, 2004]. Thus, the observations that the torus densities were larger than *Voyager* epoch data by around 35±14 percent for the cold torus and 38±14 percent for the torus beyond 5.5 R_J (ribbon, warm torus, extended torus) are consistent with observations.

Returning to the development of Model G, the fitted scale heights for the cold torus and the torus beyond 5.5 R_J were 44±15 percent and 2± 9 percent, respectively, greater for Model F than Model B. Consequently, the scale height for the cold torus is 44±15 percent greater for Model G than Model B and the scale heights for the ribbon, warm, torus, and extended torus are 2± 9 percent greater for Model G than Model B.

These scale heights can be interpreted in terms of the ion temperature of plasma in the torus. In the IPT, the plasma has a diffusive equilibrium distribution along magnetic field lines for a multi-species plasma [*Angerami and Thomas*, 1964; *Bagenal*, 1994; *Dougherty et al.*, 2017]. This can be approximated by a simple scale height distribution [*Thomas et al.*, 2004]. The scale heights are related to ion temperature, as follows [*Phipps and Withers*, 2017]:

$$T = H^2 \frac{3\Omega^2 < M >}{2k_B}. \tag{6}$$

Here T is the perpendicular ion temperature, H is the scale height, Ω is the Jupiter rotation rate (corresponding to a period of 9.925 hours), $< M >$ is the mean molecular weight of the ion species in the region of interest, and k_B is the Boltzmann constant. We assume that the compositions of IPT regions during PJ1 are consistent with previous in situ and remote sensing spectroscopic observations and have the mean ion masses reported in Table 3 [*Nerney et al.*, 2017]. With this assumption, temperatures can be inferred from the fitted scale heights. Temperatures are reported in Table 3.

These ion temperatures are larger in the cold torus and similar in the warm torus compared to values from the *Voyager* epoch (third column in Table 1). The *Ulysses* spacecraft found parallel ion temperatures around a factor of 2 less than the *Voyager* era, which translates to a scale height around 30 percent smaller [*Bird et al.*, 1993]. Ground-based observations of the torus show warm torus ion temperatures of around 70 eV at 5.89 R_J and cold torus ion temperatures of around 5–6 eV [*Thomas et al.*, 2001, 2004; *Herbert et al.*, 2008; *Bagenal et al.*, 2017b]. Thus, the derived temperatures from *Juno* observation from PJ1 are consistent with some previous observations, but not the *Voyager* cold torus observations.

A comparison of PJ1 TEC values observed by *Juno* and predicted by Model G is shown in Figure 9. This model includes a tilt of 8.0 degrees for the warm torus and 7.2 degrees for the cold torus from the rotational equator.

7. Summary

Juno Perijove 1 occurred on 27 August 2016 at 13:44 UTC Earth Received Time. Over the course of this pass, the spacecraft was receiving X-band singals and re-transmitting at X-band and Ka-band frequencies [*Folkner et al.*, 2017]. These downlinks passed through the Io plasma torus. The frequencies received by the Deep Space Network have been used to derive the total electron content along the path between *Juno* and Earth. Calibration for the Earth's ionosphere and the interplanetary medium results in a time series of the Io plasma torus total electron content.

The Io plasma torus total electron content is used, in conjunction with models made with *Voyager* data [*Phipps and Withers*, 2017], to determine the scale height and peak density of the Io plasma torus. The plasma densities were found to be larger (38±14 percent for the warm torus and 35±14 percent for the cold torus) than those recorded during the *Voyager* epoch. The scale heights are used to determine the ion temperatures assuming constant average ion mass for each region [*Thomas et al.*, 2004]. The ion temperatures derived for the derived scale heights are consistent with Earth-based observations. For the cold torus the values are 2.0 ± 0.5 times those recorded by *Voyager* while the warm torus values are similar. Comparison to the models also shows that there appears to be a departure from nominal torus tilt (1.7±0.2 degrees for the warm torus and 0.9±0.1 degrees for the cold torus). This is similar to the torus offset found by *Herbert et al.* [2008] where they found that the ribbon was tilted relative to the cold torus by 1–2 degrees.

The departure from *Voyager* epoch models gives rise to several questions that remain to be answered. First, what is the cause of the departure from nominal dipole centrifugal coordinates? *Bagenal* [1994] discussed the dependence of torus geometry on magnetic field models and their higher-order moments. Magnetic field measurements from the *Juno* spacecraft will lead to better models of the magnetic field that can be used for comparison to TEC observations. Second, How does the temperature and density found from TEC observations vary between Perijoves? Variations with System III longitude and time have been found from *Cassini* ultraviolet observations [*Steffl et al.*, 2006, 2008] and Earth-based observations [*Thomas et al.*, 2001; *Nozawa et al.*, 2004; *Tsuchiya et al.*, 2015]. Third, what environmental factors could be causing any changes found? Variations in the torus ultraviolet intensities with Io phase angle and local time have been found by

HISAKI [*Tsuchiya et al.*, 2015]. Similar observations during subsequent *Juno* perijove passes will help address these questions.

Acknowledgments. The authors would like to thank Fran Bagenal and Parker Hinton for useful discussions pertaining to the *Voyager* and magnetic field models. The authors would like to thank Michael Bird and an anonymous referee for their suggestions. This work was supported in part via a NASA JPL Education Office internship with the JPL Radio Science Systems Group and by NASA award NNX15AI87G. This work was partially carried out at the Jet Propulsion Laboratory, California Institute of Technology, under a contract with the National Aeronautics and Space Administration. The data used in this work are publicly available on the NASA Planetary Data System at http://pds-atmospheres.nmsu.edu/data_and_services/atmospheres_data/JUNO/gravity.html.

References

Angerami, J. J., and J. O. Thomas (1964), Studies of Planetary Atmospheres, 1, The Distribution of Electrons and Ions in the Earth's Exosphere, *J. Geophys. Res.*, *69*, 4537–4560, doi:10.1029/JZ069i021p04537.

Asmar, S. W., S. J. Bolton, D. R. Buccino, T. P. Cornish, W. M. Folkner, R. Formaro, L. Iess, A. P. Jongeling, D. K. Lewis, A. P. Mittskus, R. Mukai, and L. Simone (2017), The Juno Gravity Science Instrument, *Space Sci. Rev.*, *213*, 205–218, doi:10.1007/s11214-017-0428-7.

Bagenal, F. (1994), Empirical model of the Io plasma torus: Voyager measurements, *J. Geophys. Res.*, *99*, 11,043–11,062, doi:10.1029/93JA02908.

Bagenal, F., and P. A. Delamere (2011), Flow of mass and energy in the magnetospheres of Jupiter and Saturn, *J. Geophys. Res.*, *116*, A05209, doi:10.1029/2010JA016294.

Bagenal, F., and J. D. Sullivan (1981), Direct plasma measurements in the Io torus and inner magnetosphere of Jupiter, *J. Geophys. Res.*, *86*, 8447–8466, doi: 10.1029/JA086iA10p08447.

Bagenal, F., A. Adriani, F. Allegrini, S. J. Bolton, B. Bonfond, E. J. Bunce, J. E. P. Connerney, S. W. H. Cowley, R. W. Ebert, G. R. Gladstone, C. J. Hansen, W. S. Kurth, S. M. Levin, B. H. Mauk, D. J. McComas, C. P. Paranicas, D. Santos-Costa, R. M. Thorne, P. Valek, J. H. Waite, and P. Zarka (2017a), Magnetospheric Science Objectives of the Juno Mission, *Space Sci. Rev.*, *213*, 219–287, doi:10.1007/s11214-014-0036-8.

Bagenal, F., L. P. Dougherty, K. M. Bodisch, J. D. Richardson, and J. M. Belcher (2017b), Survey of Voyager plasma science ions at Jupiter: 1. Analysis method, *Journal of Geophysical Research (Space Physics)*, *122*, 8241–8256, doi:10.1002/2016JA023797.

Bird, M. K., S. W. Asmar, J. P. Brenkle, P. Edenhofer, O. Funke, M. Paetzold, and H. Volland (1992), Ulysses radio occultation observations of the Io plasma torus during the Jupiter encounter, *Science*, *257*, 1531–1535, doi:10.1126/science.257.5076.1531.

Bird, M. K., S. W. Asmar, P. Edenhofer, O. Funke, M. Pätzold, and H. Volland (1993), The structure of Jupiter's Io plasma torus inferred from Ulysses radio occultation observations, *Planet. Space Sci.*, *41*, 999–1010, doi:10.1016/0032-0633(93)90104-A.

Bolton, S. J., F. Bagenal, M. Blanc, T. Cassidy, E. Chané, C. Jackman, X. Jia, A. Kotova, N. Krupp, A. Milillo, C. Plainaki, H. T. Smith, and H. Waite (2015), Jupiter's Magnetosphere: Plasma Sources and Transport, *Space Sci. Rev.*, *192*, 209–236, doi: 10.1007/s11214-015-0184-5.

Bolton, S. J., J. Lunine, D. Stevenson, J. E. P. Connerney, S. Levin, T. C. Owen, F. Bagenal, D. Gautier, A. P. Ingersoll, G. S. Orton, T. Guillot, W. Hubbard, J. Bloxham, A. Coradini, S. K. Stephens, P. Mokashi, R. Thorne, and R. Thorpe (2017), The Juno Mission, *Space Sci. Rev.*, *213*, 5–37, doi:10.1007/s11214-017-0429-6.

Buccino, D. R. (2016), Juno Jupiter Gravity Science Raw Data Set V1.0, JUNO-J-RSS-1-JUGR-V1.0, NASA Planetary Data System, http://pds-atmospheres.nmsu.edu/data_and_services/atmospheres_data/JUNO/gravity.html.

Campbell, J. K., and S. P. Synnott (1985), Gravity field of the Jovian system from Pioneer and Voyager tracking data, *Astron. J*, *90*, 364–372, doi:10.1086/113741.

Connerney, J. E. P., M. H. Acuña, N. F. Ness, and T. Satoh (1998), New models of Jupiter's magnetic field constrained by the Io flux tube footprint, *J. Geophys. Res.*, *103*, 11,929–11,940, doi:10.1029/97JA03726.

Dessler, A. J. (2002), *Physics of the Jovian Magnetosphere*, pp. 438–441, Cambridge, UK: Cambridge University Press.

Dougherty, L. P., K. M. Bodisch, and F. Bagenal (2017), Survey of Voyager plasma science ions at Jupiter: 2. Heavy ions, *Journal of Geophysical Research (Space Physics)*, *122*, 8257–8276, doi:10.1002/2017JA024053.

Eshleman, V. R., G. L. Tyler, G. E. Wood, G. F. Lindal, J. D. Anderson, G. S. Levy, and T. A. Croft (1979), Radio science with Voyager at Jupiter — Initial Voyager 2 results and a Voyager 1 measure of the Io torus, *Science*, *206*, 959–962, doi:10.1126/science.206.4421.959.

Folkner, W. M., L. Iess, J. D. Anderson, S. W. Asmar, D. R. Buccino, D. Durante, M. Feldman, L. Gomez Casajus, M. Gregnanin, A. Milani, M. Parisi, R. Park, D. Serra,

G. Tommei, P. Tortora, M. Zannoni, S. J. Bolton, J. E. P. Connerney, and S. M. Levin (2017), Jupiter gravity field estimated from the first two Juno orbits, *Geophys. Res. Lett.*, *44*, doi:10.1002/2017GL073140.

Foreman-Mackey, D., D. W. Hogg, D. Lang, and J. Goodman (2013), emcee: The MCMC Hammer, *Publ. A. S. P.*, *125*, 306–312, doi:10.1086/670067.

Grodent, D., B. Bonfond, J.-C. GéRard, A. Radioti, J. Gustin, J. T. Clarke, J. Nichols, and J. E. P. Connerney (2008), Auroral evidence of a localized magnetic anomaly in Jupiter's northern hemisphere, *Journal of Geophysical Research (Space Physics)*, *113*, A09201, doi:10.1029/2008JA013185.

Herbert, F., N. M. Schneider, and A. J. Dessler (2008), New description of Io's cold plasma torus, *Journal of Geophysical Research (Space Physics)*, *113*, A01208, doi: 10.1029/2007JA012555.

Hess, S. L. G., B. Bonfond, P. Zarka, and D. Grodent (2011), Model of the jovian magnetic field topology constrained by the io auroral emissions, *Journal of Geophysical Research: Space Physics*, *116*, A05,217, doi:10.1029/2010JA016262.

Hill, T. W., A. J. Dessler, and F. C. Michel (1974), Configuration of the Jovian magnetosphere, *Geophys. Res. Lett*, *1*, 3–6, doi:10.1029/GL001i001p00003.

Khurana, K. K., M. G. Kivelson, V. M. Vasyliunas, N. Krupp, J. Woch, A. Lagg, B. H. Mauk, and W. S. Kurth (2004), *The configuration of Jupiter's magnetosphere*, pp. 593–616, Cambridge, UK: Cambridge University Press.

Levy, G. S., D. W. Green, H. N. Royden, G. E. Wood, and G. L. Tyler (1981), Dispersive Doppler measurement of the electron content of the torus of Io, *J. Geophys. Res.*, *86*, 8467–8470, doi:10.1029/JA086iA10p08467.

Machuzak, R. (2008), TRK-2-23 Media Calbration Interface Document, Jet Propulsion Laboratory, Pasadena, CA., Available at https://sbn.psi.edu/archive/dawn/grav/DWNVGRS_0/DOCUMENT/TRK-2-23_REVC_L5.PDF.

Mendillo, M., X. Pi, S. Smith, C. Martinis, J. Wilson, and D. Hinson (2004), Ionospheric effects upon a satellite navigation system at Mars, *Radio Science*, *39*, RS2028, doi: 10.1029/2003RS002933.

Mukai, R., D. Hansen, A. Mittskus, J. Taylor, and M. Danos (2012), Juno Telecommunications, in *Design and Performance Summary Series*, 16, http://descanso.jpl.nasa.gov/DPSummary/summary.html.

Nerney, E. G., F. Bagenal, and A. J. Steffl (2017), Io plasma torus ion composition: Voyager, Galileo, and Cassini, *Journal of Geophysical Research (Space Physics)*, *122*, 727–744, doi:10.1002/2016JA023306.

Nozawa, H., H. Misawa, S. Takahashi, A. Morioka, S. Okano, and R. Sood (2004), Long-term variability of [SII] emissions from the Io plasma torus between 1997 and 2000, *J. Geophys. Res.*, *109*, A07209, doi:10.1029/2003JA010241.

Phipps, P. H., and P. Withers (2017), Radio occultations of the Io plasma torus by Juno are feasible, *J. Geophys. Res. (Space Physics)*, *122*, 1731–1750, doi: 10.1002/2016JA023447.

Richardson, J. D., G. L. Siscoe, F. Bagenal, and J. D. Sullivan (1980), Time dependent plasma injection by Io, *Geophys. Res. Lett.*, *7*, 37–40, doi:10.1029/GL007i001p00037.

Smyth, W. H. (1992), Neutral cloud distribution in the Jovian system, *Advances in Space Research*, *12*, 337–346, doi:10.1016/0273-1177(92)90408-P.

Smyth, W. H., and M. R. Combi (1988), A general model for Io's neutral gas clouds. II - Application to the sodium cloud, *Astrophys. J.*, *328*, 888–918, doi:10.1086/166346.

Steffl, A. J., P. A. Delamere, and F. Bagenal (2006), Cassini UVIS observations of the Io plasma torus. III. Observations of temporal and azimuthal variability, *Icarus*, *180*, 124–140, doi:10.1016/j.icarus.2005.07.013.

Steffl, A. J., P. A. Delamere, and F. Bagenal (2008), Cassini UVIS observations of the Io plasma torus. IV. Modeling temporal and azimuthal variability, *Icarus*, *194*, 153–165, doi:10.1016/j.icarus.2007.09.019.

Thomas, N. (1993), The variability of the Io plasma torus, *J. Geophys. Res.*, *98*, 18, doi:10.1029/93JE01461.

Thomas, N., G. Lichtenberg, and M. Scotto (2001), High-resolution spectroscopy of the Io plasma torus during the Galileo mission, *J. Geophys. Res.*, *106*, 26,277–26,292, doi: 10.1029/2000JA002504.

Thomas, N., F. Bagenal, T. W. Hill, and J. K. Wilson (2004), The Io neutral clouds and plasma torus, in *Jupiter:The Planet, Satellites and Magnetosphere*, edited by F. Bagenal, T. E. Dowling, and W. B. McKinnon, pp. 561–591, Cambridge, UK: Cambridge University Press.

Thornton, C., and J. Border (2000), Radiometric Tracking Techniques for Deep-Space Navigation, in *DEEP-SPACE COMMUNICATIONS AND NAVIGATION SERIES*, vol. 1, edited by J. Yuen, Jet Propulsion Laboratory, California Institute of Technology. Available at http://descanso.jpl.nasa.gov/monograph/mono.html.

Trauger, J. T. (1984), The Jovian nebula - A post-Voyager perspective, *Science*, *226*, 337–341, doi:10.1126/science.226.4672.337.

Tsuchiya, F., M. Kagitani, K. Yoshioka, T. Kimura, G. Murakami, A. Yamazaki, H. Nozawa, Y. Kasaba, T. Sakanoi, K. Uemizu, and I. Yoshikawa (2015), Local electron heating in the Io plasma torus associated with Io from HISAKI satellite observation, *Journal of Geophysical Research (Space Physics)*, *120*, 10,317–10,333, doi: 10.1002/2015JA021420.

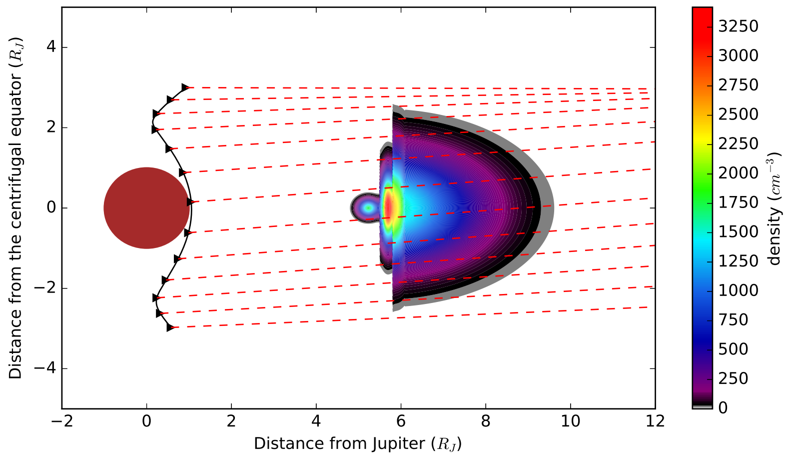

Figure 1. Illustration of the geometry of the PJ1 occultation of the Io plasma torus. Centrifugal cylindrical coordinates are used such that the vertical axis shows distance above the plane of the centrifugal equator and the horizontal axis shows distance in the plane of the centrifugal equator. The red disk at the origin shows Jupiter. Black triangles show the position of *Juno* at 1000 second intervals. The apparent reversal of Juno's motion at ±2 R_J above the centrifugal equator is not real; it is an artifact of the chosen coordinate system. Red dashed lines show lines-of-sight from Juno to Earth at the same intervals. The shaded contours show Io plasma torus electron densities Model B.

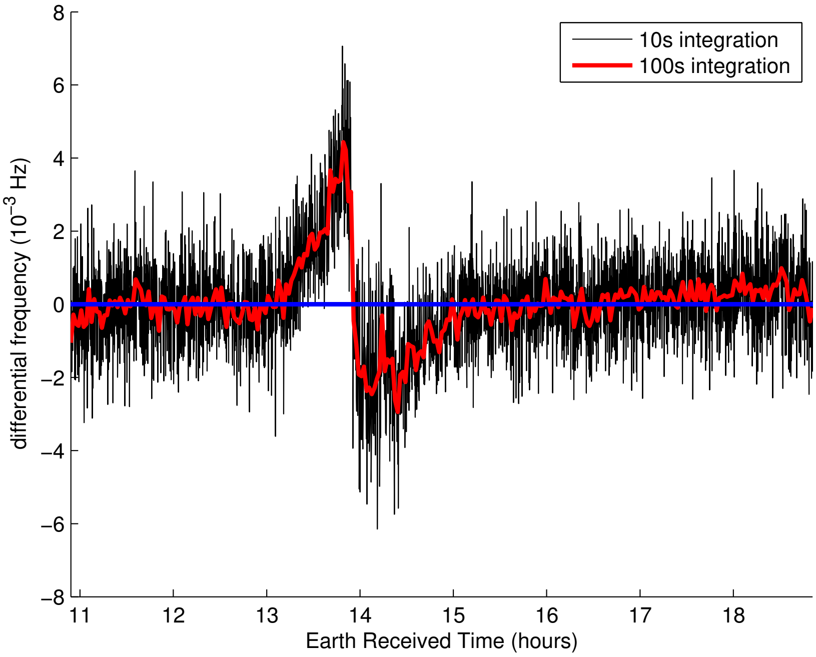

Figure 2. Differential Doppler shift from the X-band and Ka-band frequencies received at the DSN station. The black line shows the data at 10 second integration. The red dashed line shows the data at a longer integration time of 100 seconds to highlight the effects of the torus at around 13–15 hrs. The horizontal blue line indicates the location of zero.

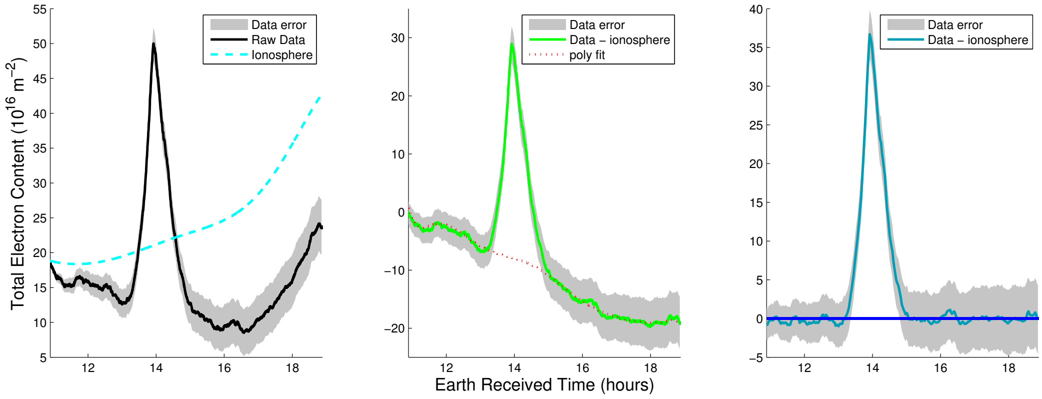

Figure 3. Calibration of total electron content profile for sources outside the Io plasma torus. (left) The black line is the original TEC profile obtained by integration of the measured frequency residuals. The cyan dashed line is the independently-measured TEC profile from Earth's ionosphere. The gray region is the error on the data. (middle) The green line is the TEC profile after subtraction of the ionospheric contribution. The red dotted line is the polynomial fit to the background. The gray region is the error on the data. (right) The blue-green line shows the TEC profile after subtraction of Earth's ionosphere and the fitted background. The horizontal blue dashed line indicates the location of zero. The gray region is the error on the data.

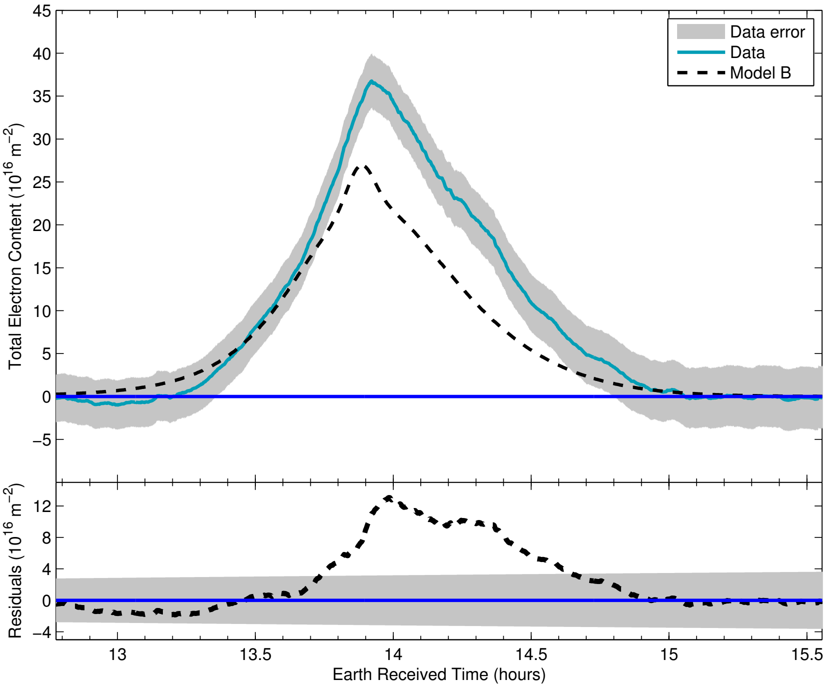

Figure 4. Comparison of *Voyager* model to TEC observations from Perijove 1. (top) The dashed black line shows the TEC time series predicted by Model B. The solid blue-green line shows the corrected TEC data and the gray region shows the error on the data. (bottom) Model-data residuals. The black dashed line shows the difference between the data and Model B. The gray region shows the error on the data. The horizontal blue line indicates zero.

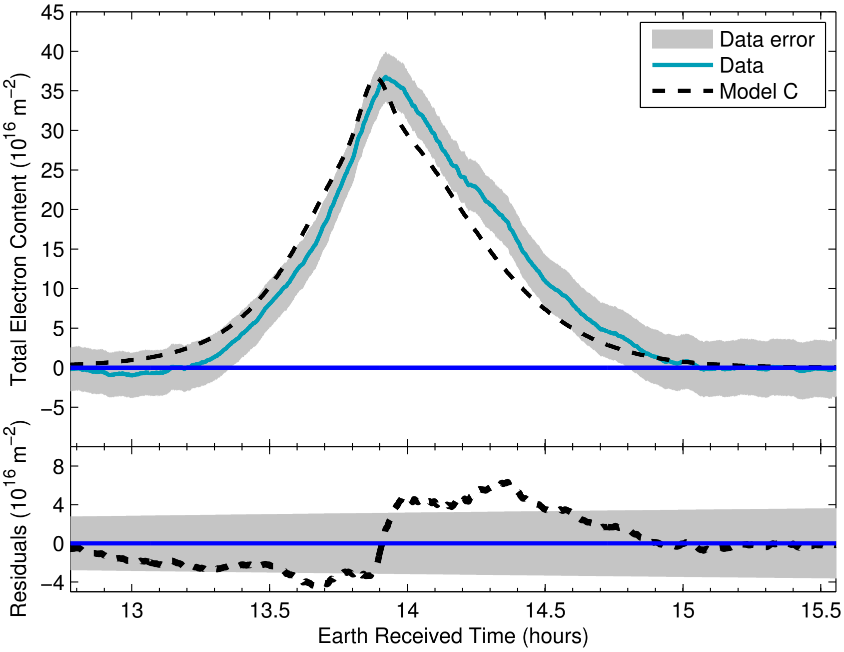

Figure 5. Comparison of rescaled *Voyager* model to TEC observations from Perijove 1. (top) The dashed black line shows the TEC time series predicted by Model C. The solid blue-green line shows the corrected TEC data and the gray region shows the error on the data. (bottom) Model-data residuals. The black dashed line shows the difference between the data and Model C. The gray region shows the error on the data. The horizontal blue line indicates zero.

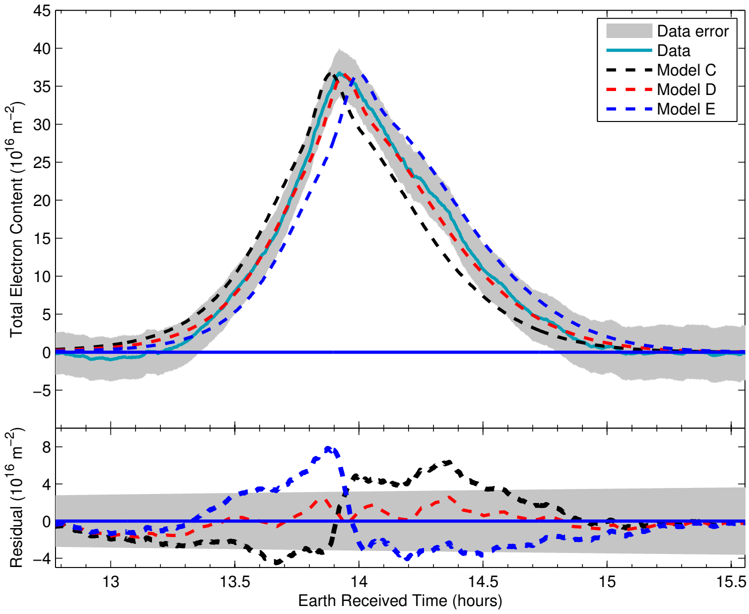

Figure 6. Effects on the TEC results of changing the tilt of the Io plasma torus. (top) The black dashed line shows the TEC profile for Model C, which has the nominal torus tilt of 6.3 degrees. The red dashed line shows the TEC profile for Model D, which minimizes the data-model residuals by adopting a torus tilt of 7.8 degrees. The blue dashed line shows the TEC profile for Model E, which adopts a torus tilt of 9.5 degrees, which is equal to the magnetic dipole tilt. The gray region shows the error on the data. The horizontal blue line indicates zero. (bottom) Corresponding plot for the data-model residuals.

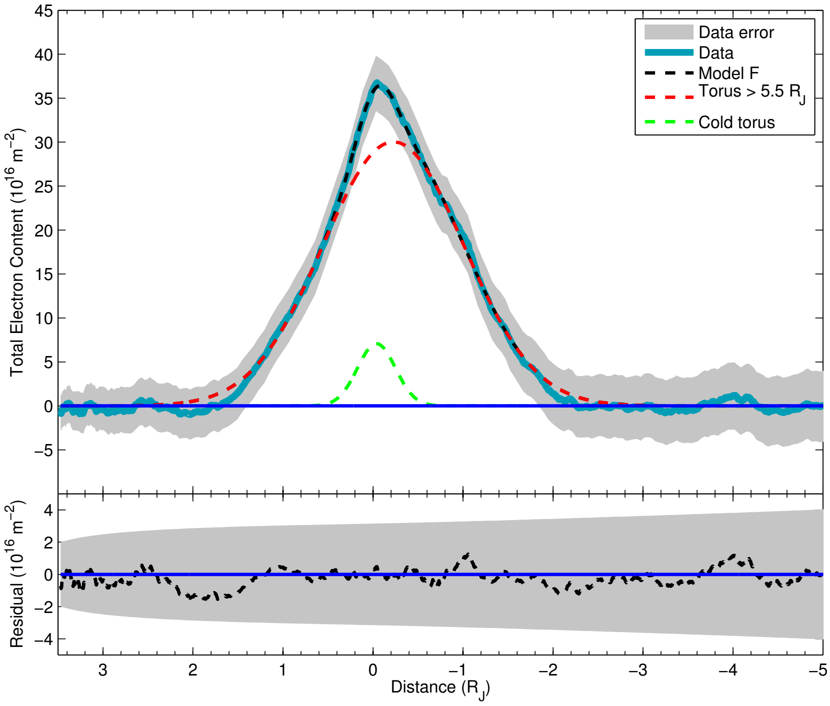

Figure 7. (top) TEC from PJ1 as a function of the z-coordinate of the line-of-sight at the point where $\sqrt{x^2 + y^2}$ equals 5.89 R_J. The blue-green line shows the data, the grey regions shows the error on the data, and the black dashed line shows Model F, which is a fit to these data. The red dashed line shows the contribution of the torus beyond 5.5 R_J to Model F. The green dashed line shows the contribution of the cold torus. The horizontal blue line indicates zero. (bottom) The black dashed line shows data-model residuals. The gray region shows the error on the data. The horizontal blue line indicates zero.

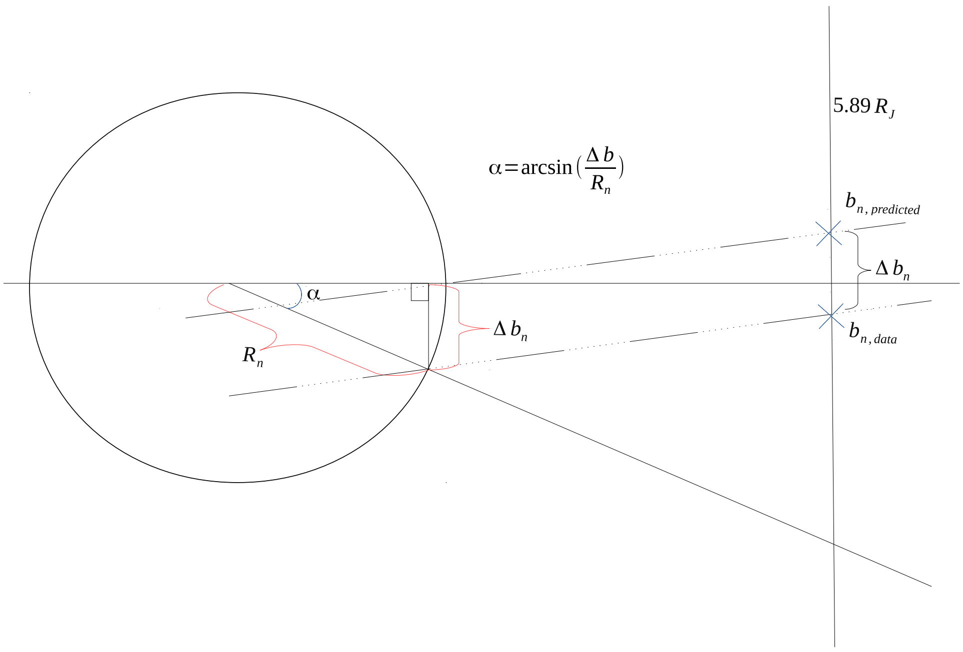

Figure 8. Geometry between lines-of-sight, the nominal centrifugal equator, the data centrifugal equator, and the perpendicular to the nominal centrifugal equator at 5.89 R_J. This also describes the relationship between the fitted b values and the angle between equators.

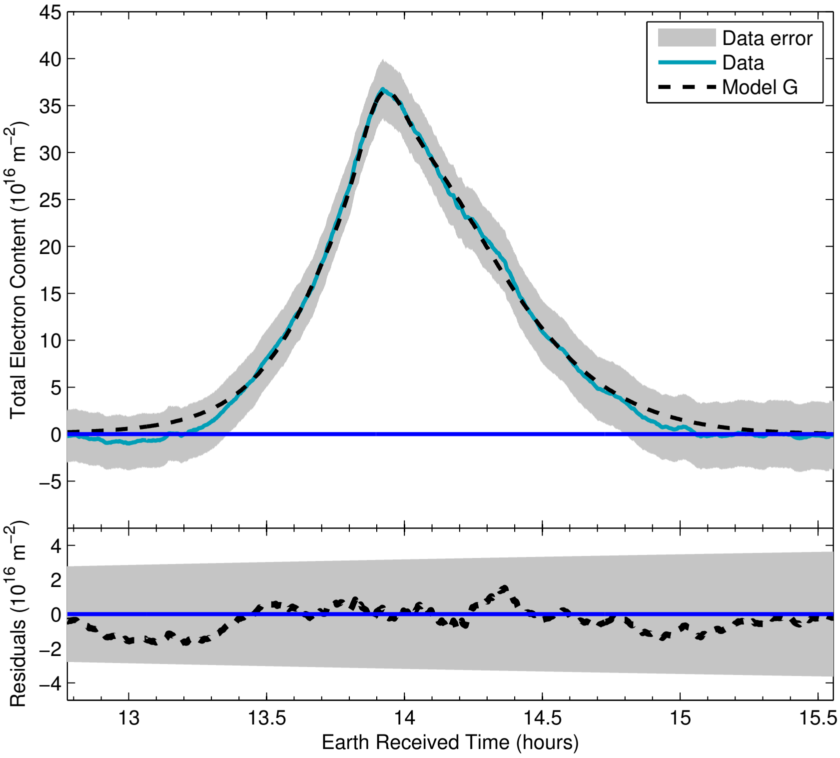

Figure 9. Comparison of TEC time series as observed and as predicted by Model G. (top) The blue-green line shows the data and the gray region shows the error on the data. The black dashed line shows Model G.The horizontal blue line indicates zero. (bottom) The blue line shows data-model residuals. The gray region shows the error on the data. The horizontal blue line indicates zero.

Table 1. Parameters for Model B.

Region	Reference Density [cm^{-3}]	Scale Height [R$_J$]	Ion Temperature [eV]	<M> [amu]	Peak Location [R$_J$]	Peak density [cm^{-3}]
Cold torus	1730	0.18	2.20	27.3	5.23	1740
Ribbon	2200	0.71	31.6	25.3	5.63	3240
Warm torus	2430	1.13	78.0	24.4	5.89	2430
Extended torus	2080	1.13	78.0	24.4	5.26	1740

<M> is mean ion mass. The peak location of the cold torus, the peak location of the warm torus, and the region widths (not listed here) are unchanged from Model A of *Phipps and Withers* [2017]. The reference densities in the second column are the coefficients for the summed Gaussian model representation of the fit to the torus density from *Voyager*. For the first three rows, the peak densities in the last column are the actual densities that would be observed at the stated peak locations. For the extended torus, the peak density in the last column is the actual density that would be observed at 6.10 R$_J$. Although the peak location for the extended torus is at 5.26 R$_J$, density contributions from the extended torus are only permitted beyond 6.10 R$_J$ in this model.

Table 2. Parameters of two-Gaussian fit to TEC profiles. predicted values are those found from a fit to the TEC profile predicted by Model B. Best-fit values are those found from a fit to the observed TEC profile (Model F). Initial values are those provided as input to the fitting routine that generated the best-fit values.

Value	Cold torus			Torus R > 5.5 R_J		
	Peak TEC a_1 TECU	Offset b_1 R_J	Scale height c_1 R_J	Peak TEC a_2 TECU	Offset b_2 R_J	Scale height c_2 R_J
Predicted	5.23	0.050	0.207	21.7	-0.042	1.09
Initial	7.01	-0.030	0.310	30.1	-0.260	1.11
Best-fit	7.07 ± 0.72	-0.038 ± 0.004	0.299 ± 0.031	30.1 ± 3.0	-0.227± 0.024	1.11 ± 0.11

Table 3. Model G.

Region	Peak Density [cm^{-3}]	Scale Height [R$_J$]	Ion Temperature [eV]	<M> [amu]	Peak Location [R$_J$]
Cold torus	2350	0.26	4.53	27.3	5.23
Ribbon	4470	0.73	33.3	25.3	5.63
Warm torus	3350	1.16	81.4	24.4	5.89
Extended torus	2401	1.16	81.4	24.4	6.10

Mean ion masses and peak locations are unchanged from Model B (Table 1). The peak location of the Extended torus is the location that the peak density would be observed rather than the location of the peak of the Gaussian in the model which we keep the same as Table 3. The implementation of the new tilts are explained in the text. Other changes are described in the text.